A Journal of the Gesellschaft Deutscher Chemiker

Angewandte International Edition GDCh Chemie

www.angewandte.org

Accepted Article

Title: Cleavage of Homonuclear Chalcogen-Chalcogen Bonds in a Hybrid Platform in Response to X-ray Radiation Potentiates Tumor Radiochemotherapy

Authors: Tianfeng Chen, Yuanyuan You, Yanzhou Chang, Shuya Pan, Qingyue Bu, Jiabao Ling, and Weiling He

To be cited as: *Angew. Chem. Int. Ed.* **2024**, e202412922

Link to VoR: https://doi.org/10.1002/anie.202412922

WILEY VCH

10.1002/anie.202412922

WILEY VCH

RESEARCH ARTICLE

Cleavage of Homonuclear Chalcogen-Chalcogen Bonds in a Hybrid Platform in Response to X-ray Radiation Potentiates Tumor Radiochemotherapy

Yuanyuan You[a,d,†], Yanzhou Chang[a,d,†], Shuya Pan[e], Qingyue Bu[a], Jiabao Ling[a], Weiling He[b,*], Tianfeng Chen[a,c,*]

[a] Y. You, Y. Chang, Q. Bu, J. Ling, Prof. T. Chen
Department of Oncology and Nano-therapeutics Institute of The First Affiliated Hospital,
College of Chemistry and Materials Science,
Jinan University, Guangzhou 510632, China.
E-mail: tchentf@jnu.edu.cn (T. Chen).

[b] Prof. W. He
Department of Gastrointestinal Surgery, The First Affiliated Hospital,
Sun Yat-sen University, Guangzhou, Guangdong 510080, China.
E-mail: wlhe@xah.xmu.edu.cn (W.L. He).

[c] Prof. T. Chen
Key Laboratory of Organosilicon Chemistry and Material Technology of Ministry of Education,
Hangzhou Normal University, Hangzhou 311121, China.

[d] Y. You, Y. Chang
Department of Orthopedics of Affiliated Hospital,
Department of Pharmacy,
Guangdong Medical University, Zhanjiang 524001, China.

[e] S. Pan
The Second Affiliated Hospital of Wenzhou Medical University,
Wenzhou Medical University, Wenzhou 325000, China.

[†]These authors contributed equally to this work.

Abstract: Chalcogens are used as sensitive redox-responsive reagents in tumor therapy. However, chalcogen bonds triggered by external ionizing radiation, rather than by internal environmental stimuli, enable site-directed and real-time drug degradation in target lesions. This approach helps to bypass chemoresistance and global systemic toxicity, presenting a significant advancement over traditional chemoradiotherapy. In this study, we fabricated a hybrid monodisperse organosilica nanoprodrug based on homonuclear single bonds (disulfide bonds (S–S, approximately 240 kJ/mol), diselenium bonds (Se–Se, approximately 172 kJ/mol), and tellurium bonds (Te–Te, 126 kJ/mol)), including ditelluride-bond-bridged MONs (DTeMSNs), diselenide-bond-bridged MONs (DSeMSNs) and disulfide-bond-bridged MONs (DSMSNs). The results demonstrated that differences in electronegativities and atomic radii influenced their oxidation sensitivities and reactivities. Tellurium, with the lowest electronegativity, showed the highest sensitivity, followed by selenium and sulfur. DTeMSNs exhibited highly responsive cleavage upon exposure to X-rays, resulting in oxidation to TeO_3^{2-}. Furthermore, chalcogen-hybridized organosilica was loaded with manganese ions (Mn^{2+}) to enhance the release of Mn^{2+} during radiotherapy, thereby activating the the stimulator of interferon genes (STING) pathway and enhancing the tumor immune response to inhibit tumor growth. This investigation of hybrid organosilica deepens our understanding of chalcogens response characteristics to radiotherapy and enriches the design principles for nanomedicine based on prodrugs.

Introduction

Clinically approved prodrugs are typically activated through chemical stimulation of the tumor microenvironment (TEM).[1] However, this endogenous chemical activation method may lead to off-target toxicity and poor responsiveness, making traditional chemotherapy encounter numerous obstacles, including severe side effects and limited efficacy.[2] In contrast, prodrugs that respond to external stimuli are expected to resolve this bottleneck.[3] The universality, high tissue penetration and tumor targeting of radiotherapy make X-ray (or γ-ray) the best external stimulus to control nanodrug release thus to maximize local efficacy,[4] overcome resistance to traditional drugs and reduce systemic toxicity.[5] However, developing prodrugs with strong specificity and sensitivity to X-ray to overcome the shortcomings of traditional chemoradiotherapy remains a huge challenge.[6]

Chalcogens (S, Se, and Te) have been explored as redox-responsive reagents in tumor therapy due to their enhanced radiation response capabilities.[4c, 7] Xu et al. constructed a series of diselenide-bond-containing nanoparticles, where diselenide-bonds could be interrupted and oxidized to form selenite, which is highly toxic to tumor cells upon gamma (γ)-radiation.[8] Liang et al. developed a diselenide-bridged mesoporous silicon material that degrades in response to TME for drug release through low-dose X-ray-triggered matrix disintegration, indicating its potential as a drug carrier for combined X-ray-mediated chemotherapy,

10.1002/anie.202412922

radiotherapy and immunotherapy. [9] In comparison, the Te–Te bond, with lower bond energy than Se–Se and S–S bonds (S–S: 240 kJ/mol, Se–Se: 172 kJ/mol, and Te–Te: 126 kJ/mol),[10] demonstrates greater chemical activity,[11] and exhibits an even stronger redox reaction sensitivity than the Se–Se bond.[12] Despite advancements in biomedicine, research on tellurium remains limited, particularly concerning Te–Te ditellurium bonds. Only a few polymers containing ditellurium functional groups have been reported for tumor treatment.[13] Despite these advances, research on chalcogen-chalcogen-based X-ray-responsive drug platforms is still emerging. Revealing the sensitivity differences and reaction rules of chalcogen-chalcogen bonds response to X-ray radiations is helpful to guide drug design principles, which is essential for developing new chalcogen-based drugs for clinical applications.

In this study, S–S, Se–Se, and Te–Te bonds were incorporated into hybrid mesoporous silica (MON) to construct ditelluride-bond-bridged MONs (DTeMSNs), diselenide-bond-bridged MONs (DSeMSNs), and disulfide-bond-bridged MONs (DSMSNs). The sensitivity of these bonds to radiotherapy was investigated. Based on the differences in their electronegativities and atomic radii, the results showed varying oxidation sensitivities and reactivities (DTeMSNs > DSeMSNs > DSMSNs). The morphology of DSMSNs showed minimal changes, whereas the bridged DSeMSNs exhibited partial cleavage. The organic silica-containing ditelluride bonds (DTeMSNs) demonstrated highly responsive cleavage to X-rays, resulting in oxidation to TeO_3^{2-} and exerting its chemotherapy effect (**Scheme 1**). Additionally, telluride hybrid organosilica was loaded with Mn^{2+}, which was released at specific locations during radiotherapy, activating the stimulator of interferon genes (STING) pathway within the tumor and enhancing the immune response of the body.

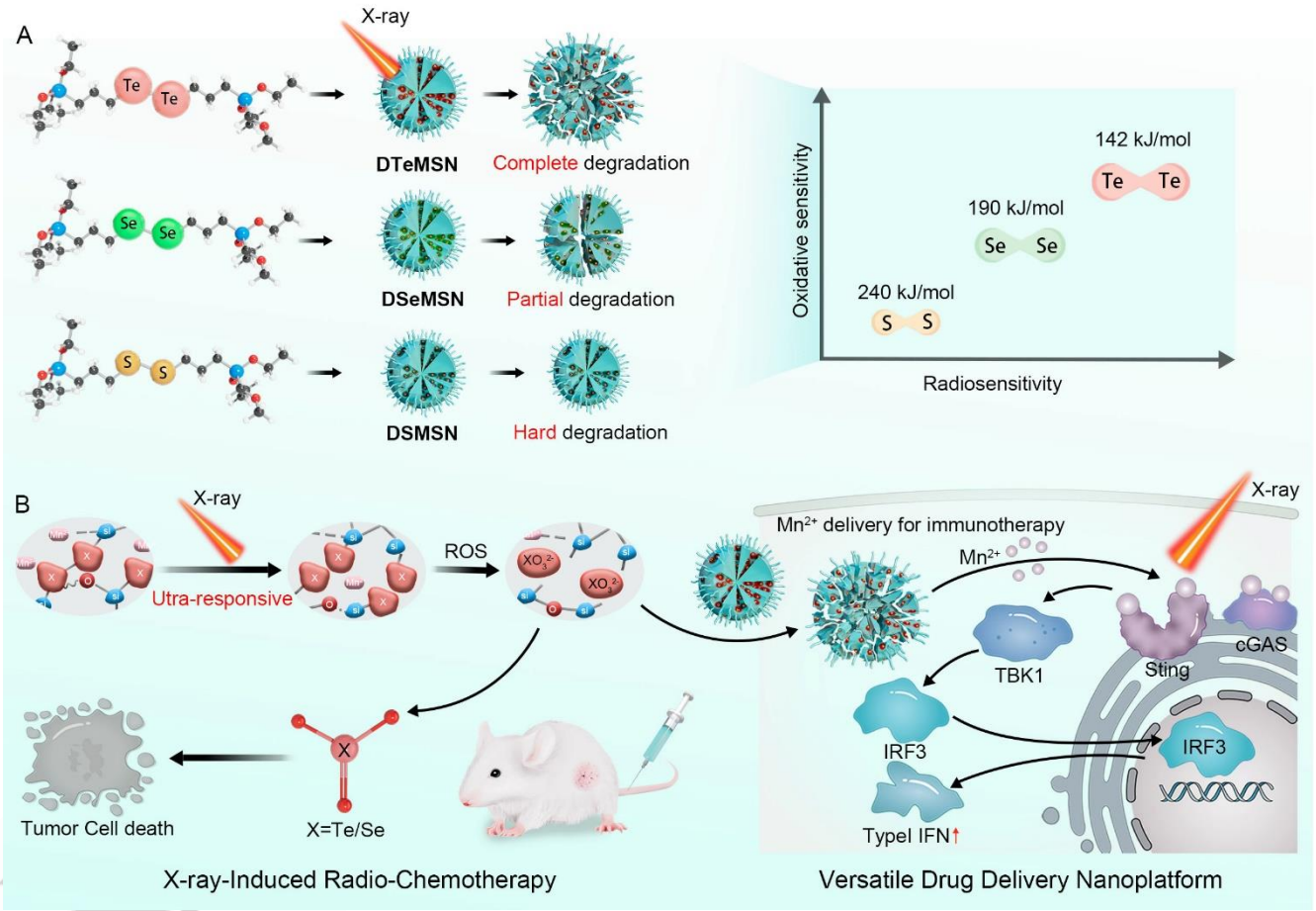

Scheme 1. Diagram of X-ray ultra-responsive homonuclear chalcogen-based nanoplatform for tumor radio-chemotherapy.

Results and Discussion

Ditelluride-bond-containing, diselenium-bond-containing, and disulfide-bond-containing organosilica precursors were synthesized and characterized using ^{1}H, ^{13}C, and mass spectrometry (MS) (**Figure S1-S4**). Organic-inorganic hybrid MON, including ditelluride-bond-bridged DTeMSNs, diselenide-bond-bridged DSeMSNs, and disulfide-bond-bridged DSMSNs, were prepared by a modified sol–gel approach, incorporating ditellurium, diselenium, and disulfide bonds into the structural framework of MONs (**Figure 1A**). Transmission electron microscopy (TEM) images revealed monodisperse, spherical DSMSNs, DSeMSNs, and DTeMSNs particles with a diameter of approximately 50 nm, along with mesopores. TEM-energy dispersive spectrometry (EDS) analysis clearly demonstrated the

10.1002/anie.202412922

distribution of chalcogenide elements Te, Se, and S (**Figure 1B, Figure S5**).

The X-ray Photoelectron Spectroscopy (XPS) characteristic peaks of the Te 3d orbital in DTeMSNs, the Se 3d orbital in DSeMSNs and the S 2p orbital in DSMSNs further confirmed the existence of ditellurium, diselenide and disulfide bonds, but shift slightly to high fields due to the existence of Te-C, Se-C and S-C bonds in organosilica (**Figure 1C-E**). Then, the Raman spectra of DSMSNs, DSeMSNs, and DTeMSNs confirmed the existence of S-S, Se-Se, and Te-Te bonds (**Figure S6**). X-ray diffraction (XRD) analysis indicated that the prepared nanosystem was amorphous (**Figure 1F**). The N_2 adsorption-desorption isotherms of the three types of MONs and mesoporous silica microsphere (MSNs) demonstrated similar type-IV isotherms (**Figure 1G,1H and S7**). The Brunauer-Emmett-Teller (BET) surface area of DTeMSNs was 296.1798 m^2 g^{-1}, with a total pore volume of 0.99 cm^3 g^{-1}. DTeMSNs, DSeMSNs, and DSMSNs have a small pore size with an average distribution centered at 3.8 nm, 3.3 nm and 3.8 nm, respectively, which facilitates drug delivery. Te, Se, and S contents of MON were determined by inductively coupled plasma MS (ICP-MS) to be 9.8%, 8.9%, and 10.6%, respectively. The zeta potentials of DTeMSNs, DSeMSNs, and DSMSNs were similar (**Figure S8**), suggesting that the S-S, Se-Se, and Te-Te bonds had a minimal effect on the surface properties of the nanoparticles.

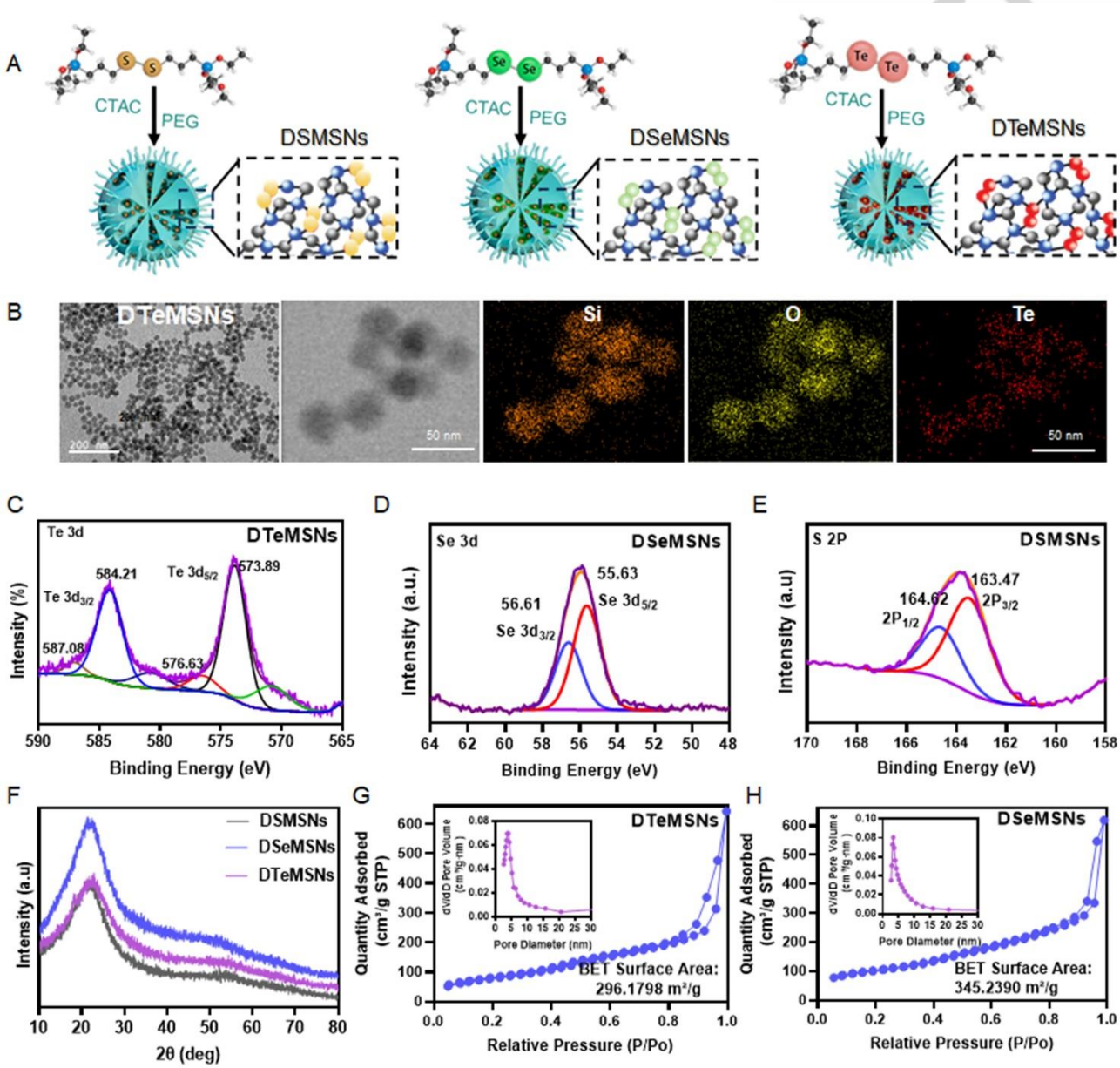

Figure 1. Synthesis and characterization of Organic-inorganic hybrid MONs. (A) Synthetic schematic of DTeMSNs, DSeMSNs, and DSMSNs. (B) High-resolution TEM images and EDS analysis of DTeMSNs. (C-E) XPS spectra of Te 3d, Se 3d, S 2p in DTeMSNs, DSeMSNs and DSMSNs. (F) XRD patterns of DSMSNs, DSeMSNs, and DTeMSNs. (G, H) N_2 adsorption-desorption isotherm curves of DTeMSNs and DSeMSNs.

10.1002/anie.202412922

RESEARCH ARTICLE

The responsiveness of nanoparticles to simulated X-ray irradiation was also investigated (**Figure 2A**). TEM images revealed that the DTeMSNs underwent rapid disintegration, both on the surface and internally, upon exposure to X-ray radiation (**Figure 2B, S9**). The DSeMSNs also exhibited partial cleavage, while minimal visible changes were observed in the morphology of the DSMSNs after irradiation. To further confirm the X-ray sensitivity of the three nanosystems, we loaded $MnCl_2$ in the three nanosystems and quantitatively analyzed the release of Mn^{2+} to reflect the cracking rate of the nanosystems. Quantitative analysis of the Mn^{2+} release showed that Mn-DTeMSNs had the fastest degradation rate under X-ray irradiation, followed by Mn-DSeMSNs (**Figure 2C**). These results show that DTeMSNs exhibits the highest sensitivity to X-rays, followed by DSeMSNs and DSMSNs.

Interestingly, X-ray radiation accelerated the decomposition of DTeMSNs and DSeMSNs under oxidative (H_2O_2) or reduced (GSH) conditions. As observed in **Figure 2D** and **2E**, DTeMSNs exhibited a tendency to cleave after incubation with H_2O_2 or GSH for 2 h. Cleavage of DSeMSNs and DSMSNs was not observed under these conditions. However, when the three nanoparticles were incubated with H_2O_2 or GSH for 2 h and then treated with X-ray, DTeMSNs were completely cleaved, and DSeMSNs and DSMSNs exhibited clear signs of cleavage. This phenomenon can be attributed to the weakening of bond energy in Te-Te, Se-Se, and S-S bonds after incubation with H_2O_2 or GSH, which was further accelerated under X-ray irradiations. The degradation products of DTeMSNs were analyzed using XPS (**Figure 2F**). The increase in Te $3d_{3/2}$ and $3d_{5/2}$ binding energies from 575 to 587 eV confirmed the formation of telluric acid TeO_3^{2-}, indicating cleavage of the ditelluride bond. These findings indicate that the Te-Te bond is the most susceptible to X-ray radiation (Te-Te > Se-Se > S-S, **Figure 2G**) due to the significant atomic radius of Te and the relatively low bond energy.

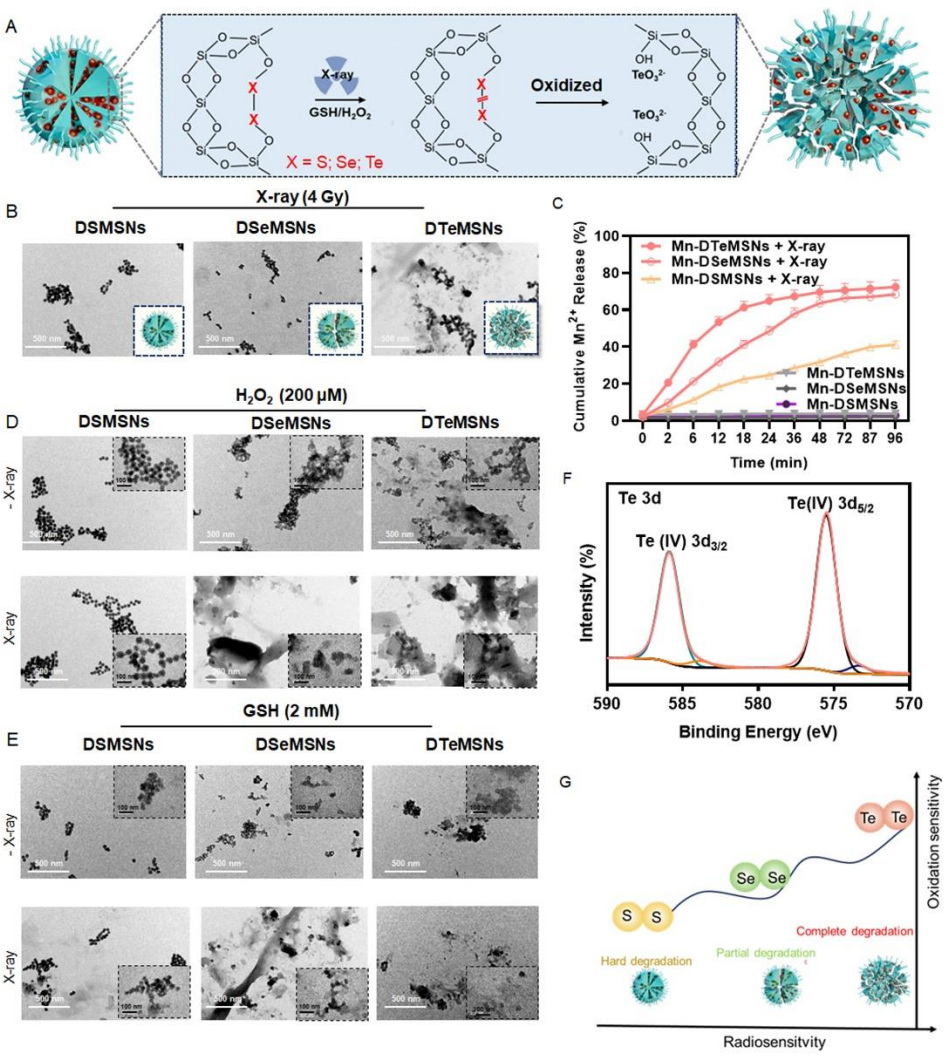

Figure 2. Evaluation of X-ray responsiveness of DTeMSNs, DSeMSNs and DSMSNs. (A) Schematic of the degradation behavior of DTeMSNs, DSeMSNs, and DSMSNs upon X-ray irradiations or simulate redox internal environment. (B) TEM images of DTeMSNs, DSeMSNs, and DSMSNs exposed to X-ray (4 Gy) irradiations. (C) Accumulated release profiles of Mn^{2+} from Mn-DTeMSNs，Mn-DSeMSNs，Mn-DSMSNs upon X-ray (4 Gy) irradiations at different time points. (D) and (E) TEM images of DTeMSNs, DSeMSNs, and DSMSNs exposed to X-ray (4 Gy) irradiations after treated with H_2O_2 (200 μM) or GSH (2 mM) for 2 h. (F) XPS spectra of Te 3d in DTeMSNs after X-ray treatment. (G) Schematic of the radiosensitvity for DTeMSNs, DSeMSNs, and DSMSNs.

10.1002/anie.202412922

RESEARCH ARTICLE

Logically, we investigated the cellular events caused by the biochemical cascade caused by the X-ray ultrasensitive properties of DTeMSNs. DTeMSNs are considered effective radiosensitizers for cancer treatment. The cytotoxicities of DTeMSNs, DSeMSNs, and DSMSNs on tumor cells were evaluated using MSN as contrast agents by MTT assay.[14] DTeMSNs, DSeMSNs, and DSMSNs showed minimal toxicity to normal breast Hs 578Bst cells (**Figure 3A**). DTeMSNs exhibited cytotoxicity toward 4T1 cells upon exposure to X-ray irradiation at doses of 2, 4, and 8 Gy, compared to the control group (**Figure 3B**). Cell viability decreased significantly in the lower doses of administration groups, but this effect was not dependent on the irradiation dose. On the contrary, DSeMSNs and DSMSNs did not demonstrate significant tumor cytotoxicity, regardless of X-ray exposure. The increased toxicity of degraded DTeMSNs to tumor cell is presumably due to the instantaneous oxidation of the Te-Te bonds broken by X-ray irradiations in the presence of excess ROS generated by the rapid proliferation of tumor cells compared with normal cells,[15] resulting in a persistent accumulation of highly toxic TeO_3^{2-} accompanied by the collapse of the DTeMSNs backbone (**Figure 3C**). Subsequently, X-ray-induced DTeMSNs-mediated radiobiological effects were also evaluated. Under radiotherapy, the levels of ROS increased in tumor cells treated with DTeMSNs, DSeMSNs, and DSMSNs, with DTeMSNs showing the highest increase (**Figure 3D**). Additionally, the combination treatment induced apoptosis in tumor cells (**Figure 3E**). Furthermore, the combination of DTeMSNs and X-rays effectively suppressed 4T1 cell colony formation (**Figure 3F**). Similarly, DTeMSNs were cytotoxic to colon cancer cells (CT26 cells) under X-ray-triggered treatment,exhibiting broad-spectrum anti-tumor activity when triggered by X-ray exposure. DTeMSNs entered CT26 cells and increased intracellular the level of ROS, further inhibiting the growth of tumor cells thus to inducing apoptosis, presenting an improved radiotherapy effect (**Figure S10-14).** The reason for lower toxicity of DSeMSNs compared to DTeMSNs is attributed to the formation of selenite (SeO_3^{2-}), which is less toxic than TeO_3^{2-}.[16]

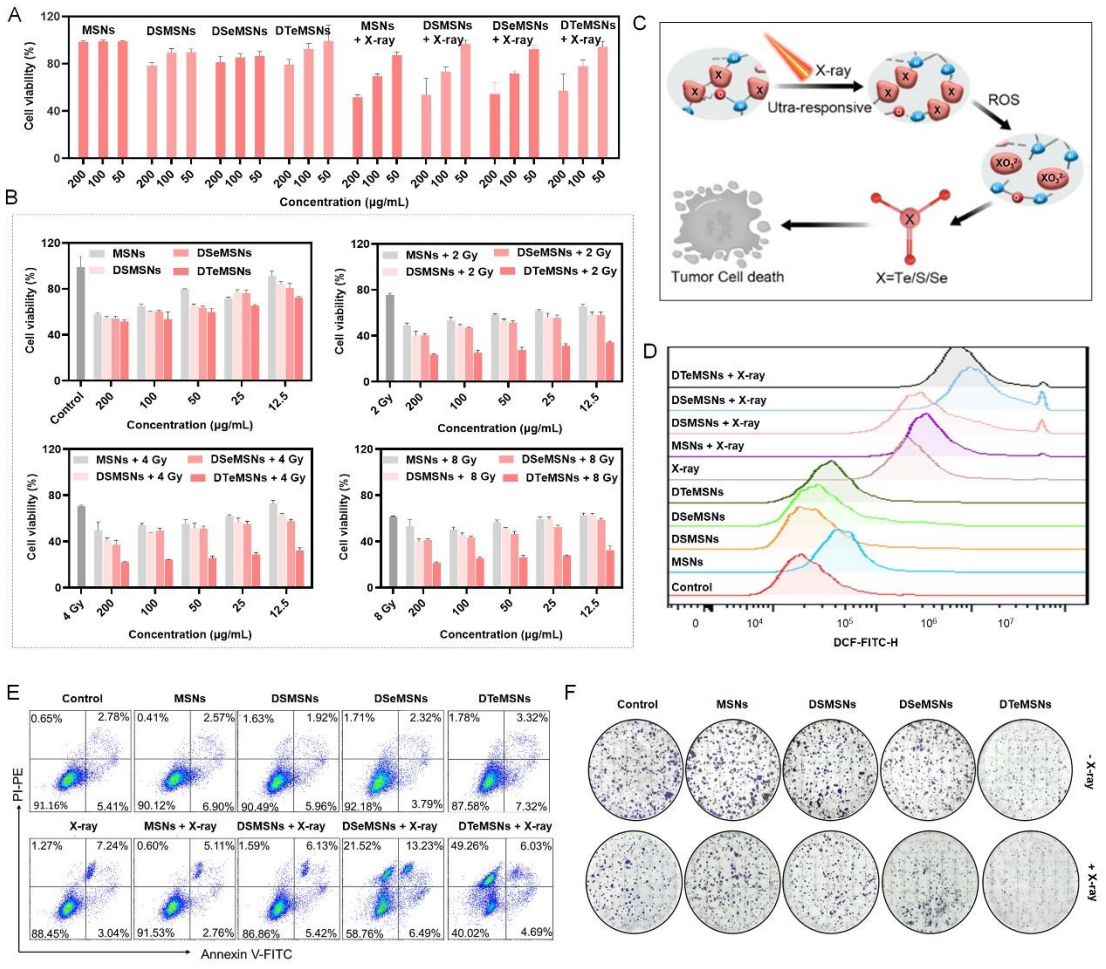

Figure 3. *In vitro* antitumor activity of DTeMSNs, DSeMSNs and DSMSNs combined with X-ray treatments. (A) Cell viability of different NPs-radiation treatment on the normal human breast cells Hs 578Bst in 72 h. The dose of X-ray was 4 Gy. (B) Cell viability of different NPs-radiation treatments on 4T1 cells in 72 h. (C) Schematic of change in DTeMSNs, DSeMSNs and DSMSNs under X-ray irradiation. (D) ROS accumulation in cells analyzed by flow cytometry. (E) Apoptosis assay of DTeMSNs, DSeMSNs and DSMSNs (100 μg/mL) determined by using Annexin V-FITC/PI staining kit. (F) Clone formation of 4T1 cells treated with DTeMSNs, DSeMSNs and DSMSNs (25 μg/mL) and X-ray. All data are shown as the mean ± S.D. (n = 3)

Benefiting from the ultraresponsiveness of DTeMSNs to X-ray irradiations and serving as excellent antitumor prodrugs, further exploration of its use as a drug carrier to achieve controlled drug release will contribute to more precise and efficient tumor treatment. Mn^{2+} are natural immune activators in cells and can initiate the STING pathway to exert antitumor immune effects. [17] Therefore, we loaded Mn^{2+} onto DTeMSNs, DSeMSNs and DSMSNs (referred to as Mn-DTeMSNs, Mn-DSeMSNs and Mn-DSMSNs, respectively) and evaluated their potential as drug carriers (**Figure 4A, Figure S15**). The loading rates of Mn^{2+} in DTeMSNs, DSeMSNs and DSMSNs, which was 25%, 23% and 20 %, respectively. We first investigated the mechanisms of Mn^{2+} loading onto DTeMSNs. To verify the existence of a bonding interaction between Mn^{2+} and DTeMSNs, we employed XPS to analyze the spectra of the 3s and 2p orbitals before and after the loading of Mn^{2+}. A binding energy difference of 6.08 eV between the characteristic peaks of the Mn 3s orbitals in $MnCl_2$, signifies that Mn is in the +2 valences state (**Figure S16**). After loading Mn^{2+} into DTeMSNs, the binding energy gap is 6.05 eV, indicating that Mn retains a valence of +2 (**Figure 4B**), but the binding energy shifts to the downfield, attributing to the transfer of electrons from Te to Mn. In addition, the tendency of the Te 3d orbital binding energy in DTeMSNs at 584.21 eV and 573.89 eV to shift towards the highfield relative to Mn-DTeMSNs at 584.50 eV and 574.07eV (**Figure 4C**), further proving the existence of Mn-Te covalent bonds. In addition, due to the negative charge of DTeMSNs, DSeMSNs, and DSMSNs and the natural adsorption characteristics of mesoporous materials, there will also be non-specific adsorption between Mn^{2+} and DTeMSNs, DSeMSNs, and DSMSNs.

Undoubtedly, the toxicity profile of the prepared nano-immune activator greatly determines their clinical fate. We then evaluated the effective safety window of Mn-DTeMSNs on bone-marrow-derived dendritic cells (BMDCs). The Mn-DTeMSNs entered BMDCs (**Figure 4D**) and maintained a relatively intact morphology even within 12 h, showing minimal cytotoxicity (**Figure S17**). However, this is opposite effect on tumor cells (**Figure S18**), which attribute to the high oxidative environment inside the tumor cells caused by rapid tumor growth.[18] As is known to all, Mn^{2+} activates the STING pathway and induces dendritic cell (DC) maturation,[19] which can directly present antigens to naïve T cells and activate the secondary immune response.[20] We then verified the *in vitro* ability of the three organic bond-bridged MONs to activate DC cells in combined with X-rays within a safe dose range. As shown in **Figure 4E** and **S19**, DSeMSNs and DTeMSNs have almost no activation effect on BMDCs, even weaker than DSMSNs, possibly due to the strong reactivity of diselenide-bonds and ditellurium-bonds that disrupt the redox balance of BMDCs. However, when loaded with Mn^{2+}, the activation effect of Mn-DTeMSNs on DCs doubled, and the activation effect on DCs was further improved in combined with X-ray irradiation, proving the excellent immunotherapeutic potential of the system. We speculate that Mn-DTeMSNs can activate MDSCs more effectively owing to the rapid cleavage and release of Mn^{2+} during radiotherapy, thereby activating the STING pathway, leading to the production of type I interferon (IFN-β),[21] and further promoting the maturation of MDSCs. [22]

Next, the transcriptional expression of the six marker gene members in the STING pathway was detected by qPCR assays. As shown in **Figure 4F**, compared with Mn-DTeMSNs, Mn-DTeMSNs combined with X-ray irradiations induced a significant up-regulation of cGAS and STING gene expression in MDSCs. However, the expression of cGAS in the BMDC treated with Mn-DSeMSNs + X-ray was relatively high, possibly due to the immune activity of Se. Additionally, the expression of IFN-β,[23] interferon regulatory factor 3 (IRF3),[24] and Toll-like receptor adapter molecule (TBK1) genes[25] was also increased. In addition, the protein expression levels of cGAS and TBK1 in BMDCs were consistent with the qPCR results (**Figure 4G, Figure S20**). Moreover, the IFN-β cytokines in the culture medium of BMDCs were significantly increased by Mn-DTeMSNs combined with radiotherapy **(Figure 4H**). These data suggest that Mn-DTeMSNs and Mn-DSeMSNs, when combined with X-rays, activate the STING pathway by releasing Mn^{2+} in response to radiotherapy, resulting in significant anticancer immune activation.

In order to evaluate the feasibility of DTeMSNs as an X-ray ultraresponsive nanodelivery, DTeMSNs was used to load Mn^{2+} to explore its anti-tumor effect using 4T1 tumor-bearing mice (**Figure 5A**). As shown in **Figure 5B**, DTeMSNs, Mn-DTeMSNs, and Mn-DSeMSNs alone did not effectively inhibit tumor growth. However, when combined with radiotherapy, Mn-DTeMSNs+X-ray exhibits a significant inhibition of tumor growth. Based on the results of primary tumor volume following treatment with different samples, we developed a standardized multiple linear regression (MLR) model,[26] represented by the equation $Y= 0.778 - 1.160X1 - 0.479X2 - 0.032X3 - 0.043X4$, where Y denotes tumor volume, and X1, X2, X3 and X4 correspond to the dosages of Mn^{2+}, DTeMSN, X-ray, and PD-L1 respectively (**Figure S21**). The regression coefficients for Mn^{2+}, DTeMSNs, and X-ray and PD-L1 in relation to tumor volume were all negative, indicating a negative correlation with tumor growth. Notably, the absolute value of the regression coefficient for X1 (1.160) is significantly higher than that for X2 (0.479) and X3 (0.032), X4 (0.043) suggesting that Mn^{2+} and DTeMSN, as key components of the nanostructures, exert the most substantial effect on suppressing tumor growth. Given the important role of DCs in both innate and adaptive immunity,[27] we examined whether X-ray-induced chemoradiotherapy could promote the maturation of DCs in the inguinal lymph nodes. As shown in **Figure 5C and S22**, the percentage of mature DCs ($CD11c^+CD80^+CD86^+$) in the Mn-DTeMSN combined with X-ray irradiations groups (43.46%) was significantly higher than that in the other treatment groups and the control group (7.81%). This percentage was comparable to that in the group treated with Mn-DTeMSNs + X-rays and anti-PD-L1 (45.52%), suggesting that this strategy promotes the maturation of DCs, priming antitumor immune responses.[28] Tumor-associated macrophages (TAMs) play a crucial role in tumor-specific immune responses.[29] As illustrated in **Figure 5D**, the proportion of M2 type macrophages in the primary tumor significantly decreased following Mn-DTeMSNs and anti-PD-1 treatment, suggesting a transformation of TAMs into M1 type macrophages.[30] In addition, treatment with Mn-DTeMSNs combined with X-ray resulted in significantly elevated levels of IFN-1β as well as CXCL10, TNF-α, IFN-γ in tumors compared to the Mn-DSMSNs + X-ray and Mn-DSeMSNs + X-ray group (**Figure 5E-G** and **S23**). By contrast, Mn-DTeMSNs, Mn-DSeMSNs, and Mn-DSMSNs individually administered groups

10.1002/anie.202412922

RESEARCH ARTICLE

did not obviously alter the secretion of TNF-α and IFN-γ. This implies that the STING pathway activation induced by Mn-DTeMSNs-mediated radiochemotherapy potentiats potent antitumor immunity. The significant effect of Mn-DTeMSNs + X-ray on tumors can be attributed to two factors: first, the breakdown of Te–Te bond in the nanosystem forms toxic substances, such as TeO_3^{2-}, which exerts the effect of chemotherapy. Second, after the Te–Te bond is broken, the Mn-DTeMSNs nanosystem releases Mn^{2+}, activating immunotherapy.

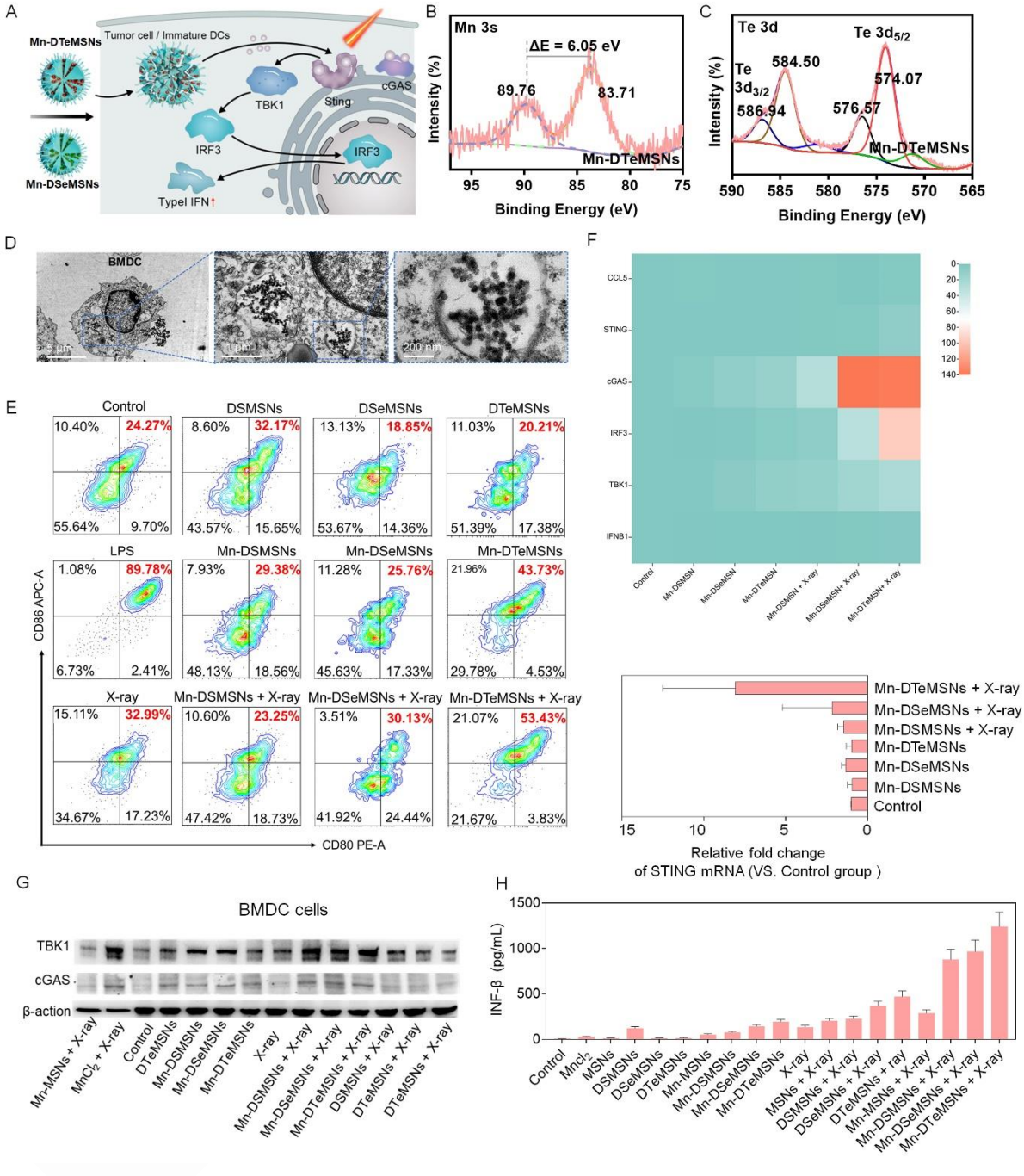

Figure 4. DTeMSNs, DSeMSNs and DSMSNs delivered Mn^{2+}activates BMDC cells. (A) Schematic of Mn^{2+} activation of BMDC cells by DTeMSNs and DSeMSNs (B) XPS spectra of the Mn 3s orbital in Mn-DTeMSNs. (C) XPS spectra of the Te 3d orbitals in Mn-DTeMSNs. (D) Bio-TEM images of 4T1 cells after co-incubation with Mn-DTeMSNs for 12 h. (E) Flow cytometry assay of matured DCs ($CD11c^+$, $CD86^+$, $CD80^+$) after co-incubation with different NPs for 24 h. (F) Heat map of STING pathway-related gene expression assessed by fluorescence real-time PCR after incubation with DTeMSNs and Mn-DTeMSNs followed by radiotherapy, and real-time PCR plots of changes in STING gene messenger RNA (mRNA) levels in BMDCs. (G) Expression of TBK1 and cGAS proteins in BMDCs. The uncropped blot was place in the supporting Information. (H) Cytokine levels of IFN-β in the medium after BMDCs treated with different nanosystem. All data are shown as mean ± S.D. (n = 3)

10.1002/anie.202412922

RESEARCH ARTICLE

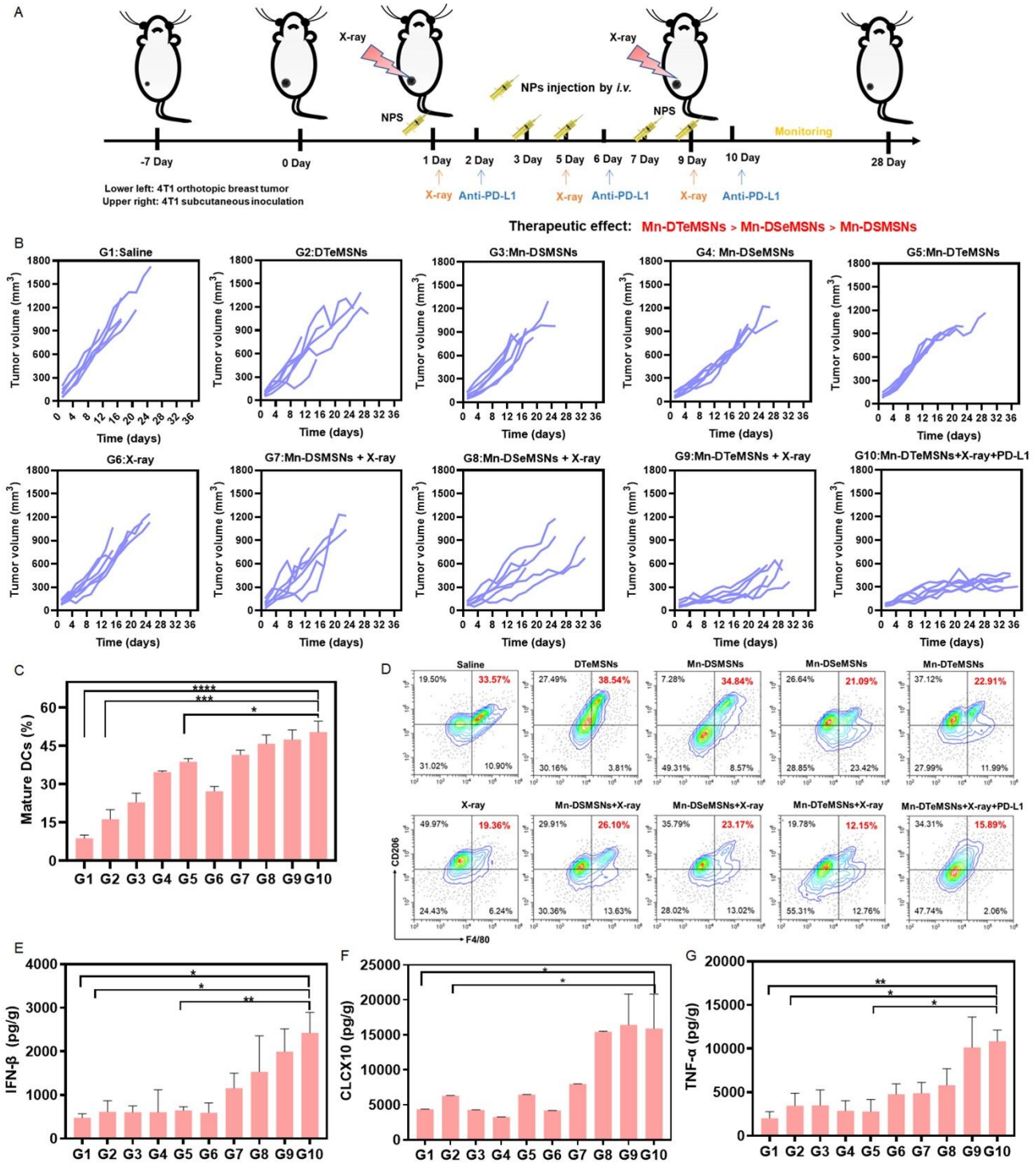

Figure 5. Mn-DTeMSNs combined with X-ray inhibit growth of tumors. (A) Schematic of the animal experimental setup for analyzing antitumor immunity of tumors. (B) Growth curves of individual primary tumor. (C) Representative flow cytometry data showing DCs maturation in inguinal lymph nodes on day 14 for different treatment groups. (D) Representative flow cytometry data of M2-like macrophages ($CD45^+CD11b^+F4/80^+CD206^+$) in tumor tissues. Cytokine expression (E) INF-β, (F) CXCL10, and (G) TNF-α in tumors. Data are shown as the mean ± S.D. (n = 3) $^*P < 0.05$, $^{**}P < 0.01$. G1, Saline; G2, DTeMSNs; G3, Mn-DSMSNs; G4, Mn-DSeMSNs; G5, Mn-DTeMSNs; G6, X-ray; G7, Mn-DSMSNs + X-ray; G8, Mn-DSeMSNs + X-ray; G9, Mn-DTeMSNs + X-ray; G10, Mn-DTeMSNs+ X-ray + PD-L1.

Tumor-specific immunity can be activated to inhibit the occurrence and development of metastatic tumors.[31] Based on the activation of tumor immunity by Mn-DTeMSNs combined with X-ray, we speculate that this approach can inhibit the growth of distant tumors. Given the high metastasis rate in breast cancer,[32] we established an orthotopic 4T1 tumor model with distal subcutaneous tumor xenografts (**Figure 6A**). Growing evidence supports anti-tumor levels Immunity is determined by a balance

10.1002/anie.202412922

of tumor-specific effectors T cells and Tregs. Therefore, we detected changes in T lymphocytes in the distant tumors across different treatment groups after 14 days of treatment (**Figure 6B**). The proportion of $CD3^+CD4^+$ Treg cells remained relatively stable, while the proportion of $CD3^+CD8^+$ CTLs significantly increased, especially in the Mn-DTeMSNs + X-ray and Mn-DTeMSNs + X-ray plus anti-PD-L1 groups. This suggests that the combination of radiotherapy and chemotherapy with immune checkpoint blockade (ICB) enhances the infiltration of CTLs into tumor tissues and revives the antitumor immune response. Additionally, the introduction of Mn^{2+} significantly reduced the proportion of MDSCs in distant tumors. Encouragingly, the synergistic effect of Mn-DTeMSNs and X-ray caused the proportion of MDSCs to decrease from 49.95% to 35.83%. In addition, when further combined with anti-PD-L1 antibodies, the proportion dropped to 22.54% (**Figure 6C** and **S24**). Similar trends were observed for M2 type TAM cells, indicating that Mn^{2+} plays a significant role in the transition from M2 to M1 in distant tumors (**Figure 6D, S25**). This was further supported by decreased IL-10 and increased IL-12 and IL-6 levels in distant tumor homogenates (**Figure S26**). These results highlight the advantages of using DTeMSNs as carriers for the complete release of Mn^{2+} under X-ray irradiation.

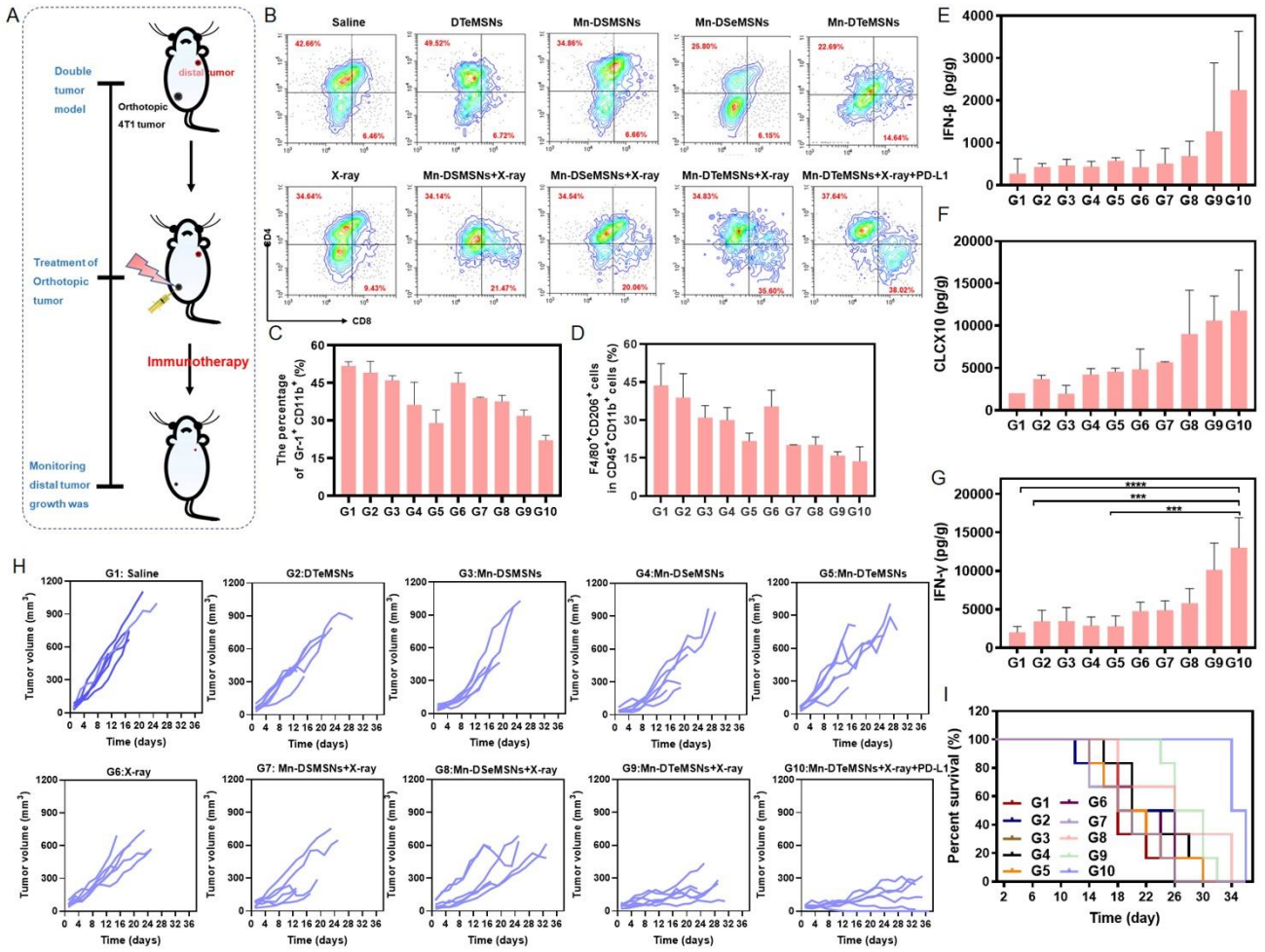

Figure 6. Mn-DTeMSNs combined with X-ray inhibits the growth of distant tumors. (A) Schematic of the animal experimental setup for analyzing antitumor immunity in distal tumors. (B) Representative flow cytometry data showing the presence of CTLs ($CD45^+CD3^+CD8^+$) and Treg cells ($CD45^+CD3^+CD4^+$) in tumor tissues. (C) Representative flow cytometry data of MDSCs ($CD45^+CD11b^+Gr\text{-}1^+$) in tumor tissues. (D) Representative flow cytometry data of M2-like macrophages ($CD45^+CD11b^+F4/80^+CD206^+$) in tumor tissues. Cytokine expression (E) INF-β, (F) CXCL10, and (G) INF-γ in distant tumors. Data are shown as mean ± S.D. (n = 3). *P < 0.05, **P < 0.01, ***P < 0.001, ****P < 0.0001. (H) Growth curves of individual distant tumors. (I) Survival curve of different treatment groups. Groups: G1, Saline; G2, DTeMSNs; G3, Mn-DSMSNs; G4, Mn-DSeMSNs; G5, Mn-DTeMSNs; G6, X-ray; G7, Mn-DSMSNs + X-ray; G8, Mn-DSeMSNs + X-ray; G9, Mn-DTeMSNs + X-ray; G10, Mn-DTeMSNs + X-ray + PD-L1.

Similarly, Mn-DTeMSNs combined with X-rays promoted the secretion of cytokines CXCL10,[33] INF-β[34] and IFN-γ[35] in distant tumors (**Figure 6E-G**), suggesting activation of the STING pathway in distant tumor. The growth curves of distal tumors in different groups of mice showed that Mn-DTeMSNs combined with X-ray had the most effective antitumor response on distant tumors (**Figure 6H**), and the combination with anti-PD-L1 not only further improved the antitumor immune response (with distal tumors completely suppressed in 1 out of 6 mice), but also prolonged the survival of the mice (**Figure 6I**). Similarly, MLR

model was also employed to analysis the contribution of Mn^{2+}, DTeMSN and X-ray, PD-L1 to inhibit the distant tumors, represented by the equation Y= 0.6 – 2.891X1 – 0.149X2 – 0.019X3 – 0.465X4. As illustrated in **Figure S27**, the regression coefficients for Mn^{2+} (X1), and DTeMSN (X2), X-ray(X3) and PD-L1(X4), in relation to tumor volume were all negative, indicating a negative correlation with tumor growth. Interestingly, the absolute value of the regression coefficient for Mn^{2+} (2.891) and PD-L1 (0.465) were significantly higher than that for primary tumor (Mn ions: 1.160; PD-L1: 0.043, **Figure S21**), suggesting that distant tumors mainly rely on Mn ions and PD-L1 enhanced tumor immunotherapy to inhibit tumor growth. This can be attributed to the conversion of Mn-DTeMSNs into highly cytotoxic telluric acid post-radiotherapy, which results in the release of Mn^{2+} and activation of the body's immune response.

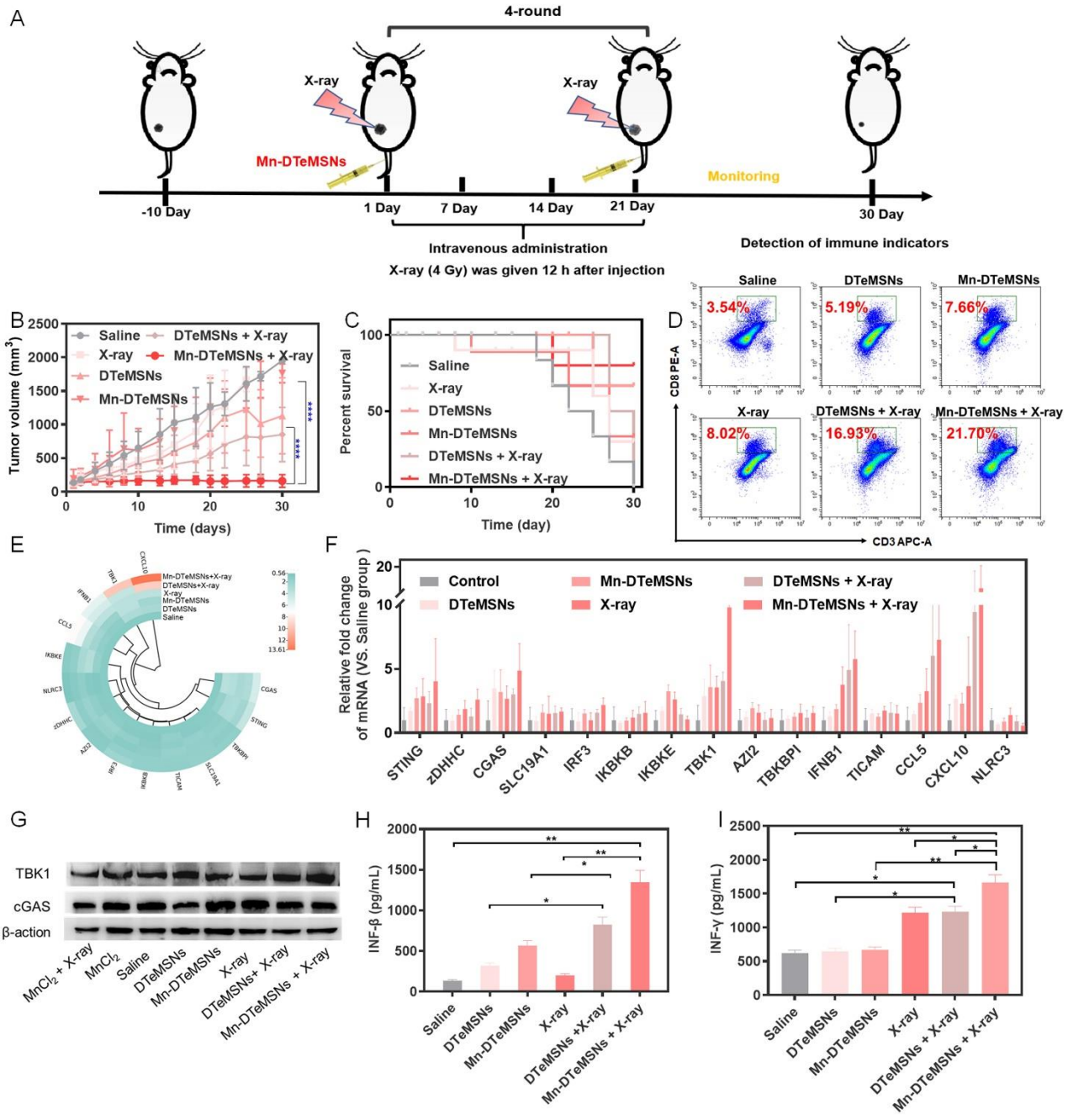

Figure 7. Mn-DTeMSN combined with X-ray activates the STING pathway. (A) Schematic of the CT26 animal experimental setup. (B) Changes in tumor volume in different groups. Data are shown as mean ± S.D. (n = 9) (C) Survival rate of each group. (D) Flow analysis of $CD3^+CD8^+$ T cells in the tumor. (E) Heat map and (F) Relative expression fold of STING pathway-related gene expression in tumor-bearing mice assessed by real-time fluorescence PCR after treatment for 30 d. (G) Western blot analysis of STING pathway-related protein expression at tumor sites. The uncropped blot was place in the supporting Information. (H) ELISA detection of IFN-β levels in serum of each group. (I) ELISA assay of IFN-γ cytokine levels in serum. Data are shown as mean ± S.D. (n = 3). *P < 0.05, **P < 0.01, ****P < 0.0001.

To further evaluate the versatility of the dichalcogen -based X-ray ultraresponsive drug platform and its expansion to different tumor models and chemoradiotherapy combinations, we established a subcutaneous CT26 tumor model to evaluate the antitumor activity of Mn-DTeMSNs (**Figure 7A**). Tumor growth curves in **Figure 7B** show that the Mn-DTeMSNs + X-ray group exhibited the most significant antitumor effect. From the mouse body weight results, it was found that these drugs showed lower toxicity in mice (**Figure S28**). The survival rate of the Mn-DTeMSNs + X-ray group was prolonged (**Figure 7C**), demonstrating both therapeutic effect and good biological safety.

We analyzed the state of T cell infiltration in the tumor areas of the mice. As shown in **Figure 7D** and **S29**, Mn-DTeMSNs alone treatments promoted the proportion of $CD8^+$ T cells as well as infiltrated $CD4^+$T cells, which was more obvious in combination of Mn-DTeMSNs and X-ray irradiations (**Figure S30**). Moreover, the number of immunosuppressive MDSC and M2 type TAM in the tumors[36] treated with Mn-DTeMSNs combined with X-rays decreased significantly (**Figure S31, Figure S32**). Naturally, the introduction of Mn^{2+} into DTeMSNs subject to X-ray exposure induced an increase in the gene expression of cGAS and STING in tumors, as well as the gene expression of IFNB1, IRF3, TBK1 and CXCL10 (**Figures 7E** and **7F**). Similarly, we detected the expression of the upstream and downstream proteins of the STING pathway (cGAS, TBK1, and p-IRF3) (**Figure 7G**). The results showed that protein expression in the X-ray, DTeMSNs + X-ray, and Mn-DTeMSNs + X-ray groups are increased, and the expression of related proteins in the Mn-DTeMSNs + X-ray group was the most upregulated. Meanwhile, the serum was obtained and marker cytokine IFN β and IFN-γ were also detected. As displayed in **Figure 7H** and **7I**, high content of IFN-β and IFN-γ were measured in DTeMSNs combined with X-ray irradiations groups relative to other treatment groups, but DTeMSNs carrying Mn^{2+} triggered the highest levels of IFN-β and IFN-γ secretion. Therefore, based on the expression of STING pathway related genes and proteins and the secretion of type I interferon IFN-β, it can be concluded that Mn-DTeMSNs combined with radiotherapy successfully awakened powerful innate immunity and reshaped the immunosuppressive microenvironment to facilitate tumor treatment.

Conclusion

In this study, homonuclear chalcogen frameworks of ditellurium-, diselenium-, and disulfide-embedded silica were constructed to explore the X-ray responsiveness of Te-Te, Se-Se, and S-S (DTeMSNs, DSeMSNs, and DSMSNs). The findings are summarized as follows: i) X-ray responsiveness of homonuclear chalcogens: The bond energies of disulfide bonds (240 kJ/mol), diselenide bonds (172 kJ/mol), and ditellurium bonds (126 kJ/mol) decrease, resulting in varying degrees of X-ray responsiveness among the chalcogen hybrid silicones (DTeMSNs > SeMSNs > DSMSNs). The introduction of ditellurium bonds can effectively improve the ultraresponsive cleavage of nanoplatforms using X-rays. ii) Chemical bond responsiveness promotes tumor radio-chemotherapy: The interrupted ditellurium bond in DTeMSNs under X-ray irradiation is converted to toxic TeO_3^{2-}, which contributes to the chemotherapeutic effect and enhances radiation therapy. iii) Excellent carrier for loading Mn^{2+} to activate the STING pathway: The cleavage of the double tellurium bond leads to the release of Mn^{2+}, which effectively activates the STING pathway in tumors, induces the production of type I interferons, and triggers innate immunity. This design provides a new paradigm for prodrug design in response to external environmental stimuli.

Acknowledgements

This work was supported by National Key R&D Program of China (2023YFC3402800), National Natural Science Foundation for Distinguished Young Scholars (82225025), National Natural Science Foundation of China (32171296, 22205080, 22305097), GuangDong Basic and Applied Basic Research Foundation (2023A1515220077, 2024A1515012842), China Postdoctoral Science Foundation (2022M710847), Postdoctoral Science Foundation of the Affiliated Hospital of Guangdong Medical University (1037Z20220053), Key Laboratory of Organosilica Chemistry and Material Technology, Ministry of Education of Zhejiang Province, Hangzhou Normal University （KFJJ2022010）.

Keywords: chalcogens • radiochemotherapy• X-ray-responsive prodrugs • nanodrugs

References

[1] a) H. Shipeng, F. Yuxin, Z. Yaojin, M. Ziyang, D. Guoqiang, S. Chunquan, *Adv. Sci.* **2024**, *11*, 2401623; b) L. Lei, F. Jiaju, Y. Jiahao, L. Lei, S. Zihao, W. Haoyu, T. Shuangjie, Z. Mingming, W. Chunru, B. Chunli, *Adv. Mater.* **2024**, *36*, 2310875; c) S. Wen, Q. Wei, L. Shu-Jin, W. Shuo, X. Jun, Y. Qi-Chao, X. Jiming, Z. Junjie, X. Zhigang, S. Zhi-Jun, *Adv. Mater.* **2022**, *35*, 2209379.

[2] Q. Fu, S. Shen, P. Sun, Z. Gu, Y. Bai, X. Wang, Z. Liu, *Chem. Soc. Rev.* **2023**, *52*, 7737–7772.

[3] a) J. Geng, Y. Zhang, Q. Gao, K. Neumann, H. Dong, H. Porter, M. Potter, H. Ren, D. Argyle, M. Bradley, *Nat. Chem.* **2021**, *13*, 805-810; b) Q. Fu, Z. Gu, S. Shen, Y. Bai, X. Wang, M. Xu, P. Sun, J. Chen, D. Li, Z. Liu, *Nat. Chem.* **2024**, 1-9.

[4] a) J. Geng, Y. Zhang, Q. Gao, K. Neumann, H. Dong, H. Porter, M. Potter, H. Ren, D. Argyle, M. Bradley, *Nat. Chem.* **2021**, *13*, 805–810; b) Shuya Pan, Guanning Huang, Zhengwei Sun, Xin Chen, Xinli Xiang, Wenxiao Jiang, Yanchao Xu, Tianfeng Chen, X. Zhu*, *Adv. Funct. Mater.* **2023**, *33*, 2213364; c) Y. Chang, J. Huang, S. Shi, L. Xu, H. Lin, T. Chen, *Adv. Mater.* **2023**, *35*, e2212178.

[5] a) Q. Zhang, X. Wang, Y. Zhao, Z. Cheng, D. Fang, Y. Liu, G. Tian, M. Li, Z. Luo, *ACS Nano* **2023**, *17*, 25419-25438; b) S. Rottenberg, C. Disler, P. Perego, *Nat. Rev. Cancer* **2021**, *21*, 37–50.

[6] D. Shao, F. Zhang, F. Chen, X. Zheng, H. Hu, C. Yang, Z. Tu, Z. Wang, Z. Chang, J. Lu, *Adv. Mater.* **2020**, *32*, 2004385.

[7] a) Y. Xu, H. Lai, S. Pan, L. Pan, T. Liu, Z. Yang, T. Chen, X. Zhu, *Biomaterials* **2023**, *305*, 122452; b) C. Shi, Z. Yuan, T. Liu, L. Chan, T. Chen, J. Zhao, *J. Mater. Chem. B* **2023**, *11*, 5607-5618; c) A. Zhang, L. Gao, *Int. J. Nanomedicine* **2023**, *18*, 6233-6256.

[8] a) D. Shao, F. Zhang, F. Chen, X. Zheng, H. Hu, C. Yang, Z. Tu, Z. Wang, Z. Chang, J. Lu, *Adv. Mater.* **2020**, *32*,

2004385; b) S. Gao, T. Li, Y. Guo, C. Sun, B. Xianyu, H. Xu, *Adv. Mater.* **2020**, *32*, 1907568.
[9] D. Shao, F. Zhang, F. Chen, X. Zheng, H. Hu, C. Yang, Z. Tu, Z. Wang, Z. Chang, J. Lu, *Adv. Mater.* **2020**, *32*, 2070372.
[10] X. Xia, J. Shi, Q. Deng, N. Xu, F. Huang, X. Xiang, *Mater. Today Chem.* **2022**, *23*, 100660.
[11] L. Wang, W. Wang, W. Cao, H. Xu, *Polym. Chem.* **2017**, *8*, 4520-4527.
[12] S. Thomas, A. Singh, A. Grosjean, K. Alhameedi, T. Grønbech, R. Piltz, A. Edwards, B. Iversen, *Angew. Chem. Int. Ed.* **2023**, *62*, e202311044.
[13] Wei, Cao, Yuwei, Gu, Tianyu, Li, Huaping, Xu, *Chem. Commun.* **2015**, *51*, 7069-7071.
[14] Y. Huang, Y. Fu, M. Li, D. Jiang, C. J. Kutyreff, J. W. Engle, X. Lan, W. Cai, T. Chen, *Angew. Chem. Int. Ed.* **2020**, *132*, 4436-4444.
[15] Z. Wang, X. Ren, Y. Li, L. Qiu, D. Wang, A. Liu, H. Liang, L. Li, B. Yang, A. K. Whittaker, *ACS Nano* **2024**, *18*, 10288-10301.
[16] S. Vávrová, E. Struhárňanská, J. Turňa, S. Stuchlík, in *Toxicology of Essential and Xenobiotic Metals*, CRC Press, **2024**, pp. 19-32.
[17] a) J. Wang, K. Mao, X. Cong, H. Tan, C. Wu, Z. Hu, Y. Yang, T. Sun, *Sci. adv.* **2022**, *8*, eabq3699; b) X. Zhou, W. Yu, S. Lyu, C. Macaubas, B. Bunning, Z. He, E. Mellins, K. Nadeau, *J. Exp. Med.* **2021**, *218*, e20201793; c) M. Koyama, G. Hill, *Blood* **2019**, *134*, 2139-2148.
[18] K. X. Teng, D. Zhang, B. K. Liu, Z. F. Liu, L. Y. Niu, Q. Z. Yang, *Angew. Chem. Int. Ed.* **2024**, *63*, e202318783.
[19] W. Zhang, L. Lu, Z. Zhu, F. Deng, W. Zhang, F. Wang, P. Zeng, H. Shi, T. Wang, Y. Chen, *Adv. Healthcare Mater.* **2024**, *13*, e2400421.
[20] a) E. Shevach, A. Thornton, *Immunol. Rev.* **2014**, *259*, 88-102; b) B. Bošnjak, K. Do, R. Förster, S. Hammerschmidt, *Immunol. Rev.* **2022**, *306*, 137-163; c) Y. Guo, P. Hu, J. Shi, *J. Am. Chem. Soc.* **2024**, *146*, 10217-10233.
[21] a) X. Zhao, K. Zhang, Y. Wang, W. Jiang, H. Cheng, Q. Wang, T. Xiang, Z. Zhang, J. Liu, J. Shi, *Adv. Funct. Mater.* **2022**, *32*, 2108883; b) P. Zhu, Y. Pu, M. Wang, W. Wu, H. Qin, J. Shi, *J. Am. Chem. Soc.* **2023**, *145*, 5803-5815.
[22] a) M. Calvet‐Mirabent, D. T. Claiborne, M. Deruaz, S. Tanno, C. Serra, C. Delgado‐Arévalo, I. Sánchez‐Cerrillo, I. de Los Santos, J. Sanz, L. García‐Fraile, *Eur. J. Immunol.* **2022**, *52*, 447-461; b) J. Yan, G. Wang, L. Xie, H. Tian, J. Li, B. Li, W. Sang, W. Li, Z. Zhang, Y. Dai, *Adv. Mater.* **2022**, *34*, 2105783.
[23] T. Mariko, L. Chan-Wang J, C. Anaamika, S. Martin, A. Ferhat, M. Matthias, G. David J, J. Mohit, S. Sonia, *Nat. Immunol.* **2021**, *22*, 485-496.
[24] R. Theresa, A. Patricia A, O. Ogooluwa, T. Lin, C. Brener, G. Luiz, C. Osvaldo, L. Philip L, F. Katherine A, H. Cole, G. Douglas T, G. Ricardo T, *Cell Metab.* **2024**, *36*, 484-497.
[25] Y. Liu, P. Xu, S. Rivara, C. Liu, J. Ricci, X. Ren, J. Hurley, A. Ablasser, *Nature* **2022**, *610*, 761-767.
[26] H. Wei, H. Lizhen, Z. Zhongyang, S. Sujiang, C. Tianfeng, *ACS Nano* **2021**, *15*, 20225-20241.
[27] a) X. He, G. Gong, M. Chen, H. Zhang, Y. Zhang, J. J. Richardson, W. Y. Chan, Y. He, J. Guo, *Angew. Chem. Int. Ed.* **2024**, *136*, e202314501; b) I. Heras-Murillo, I. Adán-Barrientos, M. Galán, S. K. Wculek, D. Sancho, *Nat. Rev. Clin. Oncol.* **2024**, *21*, 257-277.
[28] a) S. Liang, M. Liu, W. Mu, T. Gao, S. Gao, S. Fu, S. Yuan, J. Liu, Y. Liu, D. Jiang, N. Zhang, *Adv. Sci.* **2023**, *11*, 2305275; b) Y. Qian, W. Chen, M. Wang, Y. Xie, L. Qiao, Q. Sun, M. Gao, C. Li, *Small methods* **2023**, *8*, e2301231.
[29] a) C. Li, W. Zhang, Y. Nie, X. Du, C. Huang, L. Li, J. Long, X. Wang, W. Tong, L. Qin, Y. Lai, *Adv. Mater.* **2023**, e2308875; b) M. Do, W. Shi, L. Ji, E. Ladewig, X. Zhang, R. Srivastava, K. Capistrano, C. Edwards, I. Malik, B. Nixon, E. Stamatiades, M. Liu, S. Li, P. Li, C. Chou, K. Xu, T. Hsu, X. Wang, T. Chan, C. Leslie, M. Li, *Immunity* **2023**, *56*, 2555-2569.e2555.
[30] C. Li, W. Zhang, Y. Nie, X. Du, C. Huang, L. Li, J. Long, X. Wang, W. Tong, L. Qin, Y. Lai, *Adv. Mater.* **2023**, e2308875.
[31] a) W. Huang, L. He, J. Ouyang, Q. Chen, C. Liu, W. Tao, T. Chen, *Matter* **2020**, *3*, 1725-1753; b) R. Sabado, S. Balan, N. Bhardwaj, *Cell Res.* **2017**, *27*, 74-95; c) G. Gao, Y.-W. Jiang, W. Zhan, X. Liu, R. Tang, X. Sun, Y. Deng, L. Xu, G. Liang, *J. Am. Chem. Soc.* **2022**, *144*, 11897-11910.
[32] a) Y. Zhang, Y. Wang, A. Zhu, N. Yu, J. Xia, J. Li, *Angew. Chem. Int. Ed.* **2024**, *63*, e202310252; b) E. Jordan-Alejandre, A. D. Campos-Parra, D. L. Castro-López, M. B. Silva-Cázares, *Cells* **2023**, *12*, 525.
[33] X. Zhang, H. Zhang, J. Zhang, M. Yang, M. Zhu, Y. Yin, X. Fan, F. Yu, *Immunology* **2023**, *168*, 375-388.
[34] H. Wang, W. Sun, D. Zhou, Y. Qi, Z. Gao, J. Cui, D. Yu, *Chem. Eng. J.* **2024**, *480*, 148211.
[35] L. Wang, H. Zhou, Q. Chen, Z. Lin, C. Jiang, X. Chen, M. Chen, L. Liu, L. Shao, X. Liu, *Adv. Sci.* **2024**, *11*, 2307858.
[36] L. He, Q. Chen, Q. Lu, M. Yang, B. Xie, T. Chen, X. Wang, *Angew. Chem. Int. Ed.* **2024**, *63*, e202404822.

10.1002/anie.202412922

Entry for the Table of Contents

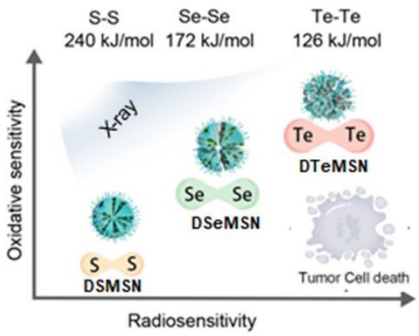

The site-directed generation of chalcogens (S, Se, Te) in response to external ionizing radiation to enable drug decaging in target lesions remains a huge challenge. Hybrid monodisperse organosilicon nanoprodrugs containing homonuclear chalcogen−chalcogen single bonds have now been developed as a versatile X-ray-ultraresponsive nanoplatform for tumor radiochemotherapy.